Delft University of Technology

Linearized 3-D Electromagnetic Contrast Source Inversion and Its Applications to Half-Space Configurations

Sun, Shilong; Kooij, Bert Jan; Yarovoy, Alexander G.

Important note
To cite this publication, please use the final published version (if applicable).
Please check the document version above.

Linearized 3-D Electromagnetic Contrast Source Inversion and Its Applications to Half-Space Configurations

Shilong Sun, Bert Jan Kooij, and Alexander G. Yarovoy, *Fellow, IEEE*

Abstract—One of the main computational drawbacks in the application of 3-D iterative inversion techniques is the requirement of solving the field quantities for the updated contrast in every iteration. In this paper, the 3-D electromagnetic inverse scattering problem is put into a discretized finite-difference frequency-domain scheme and linearized into a cascade of two linear functionals. To deal with the nonuniqueness effectively, the joint structure of the contrast sources is exploited using a sum-of-ℓ_1-norm optimization scheme. A cross-validation technique is used to check whether the optimization process is accurate enough. The total fields are, then, calculated and used to reconstruct the contrast by minimizing a cost functional defined as the sum of the data error and the state error. In this procedure, the total fields in the inversion domain are computed only once, while the quality and the accuracy of the obtained reconstructions are maintained. The novel method is applied to ground-penetrating radar imaging and through-the-wall imaging, in which the validity and the efficiency of the method are demonstrated.

Index Terms—3-D electromagnetic (EM) contrast source inversion (CSI), ℓ_1-norm regularization, cross-validation (CV), finite difference frequency domain (FDFD), ground-penetrating radar (GPR), through-the-wall (TW) imaging.

I. INTRODUCTION

ELECTROMAGNETIC (EM) inverse scattering is a procedure of recovering the characteristics of the object from the knowledge of the scattered field probed at a limited number of positions [1]. It is of great importance due to the wide spectrum of applications, such as geophysical survey [2]–[5], medical diagnosis [6]–[8], and so on. Most of the studies on the inverse scattering problems are focused on the frequencies of the resonant region, i.e., the wavelength is comparable with the dimension of the object. The research related to inverse scattering in the broad sense is still lively today due to the difficulties of dealing with the nonlinearity and ill-posedness in the Hadamard sense [9].

A variety of inversion methods have been proposed and applied to different applications during the recent decades. Very briefly, the methods can be classified into two families: 1) iterative methods and 2) noniterative methods. The contrast source inversion (CSI) method is an iterative

frequency-domain inversion method to retrieve the value of the contrast (the dielectric parameters of the scattering objects with respect to the background medium) in the testing domain, which was first proposed by van den Berg *et al.* [10]–[13], and was later applied to subsurface object detection in combination with integral equations based on the electric field integral equation formulation (see [14]). This idea was further extended to the mixed dielectric and highly conductive objects combined with CSI (see [15], [16]). To deal with the nonlinearity of the inverse problem, Chew [17]–[20] proposed the (distorted) Born iterative methods (BIMs). The key point of this method is to linearize the problem using Born's approximation and to consider the reconstructed permittivity as the inhomogeneous background. Although the iterative methods show good performance in achieving the dielectric parameters of the objects, it is extremely time-consuming for the large-scale 3-D inversion scheme with an irregular background due to the fact that each iteration involves the search of finding solutions to the updated scattering problem in the inversion domain. There is another iterative surface-based inversion method, which first parameterizes the shape of the scatterer mathematically with a number of parameters, then sequentially optimizes the parameters by minimizing a cost functional iteratively [21]. The drawbacks of this method are obvious. First, it requires *a priori* information about the position and the quantity of the scatterers. More research on this point can be found in [22] and [23]. Second, it is intractable to deal with the complicated nonconvex objects. Linear sampling method (LSM) [24], [25] is a noniterative inversion technique of finding an indicator function for each position in the region of interest (ROI) by first defining a far-field (or near-field [26]) mapping operator, and then sequentially solving a linear system of equations. We refer to [27] for the application of LSM in ground-penetrating radar (GPR). Although LSM has been proved to be effective for highly conductive scatterers and, in some cases, also applicable to dielectric scatterers [28], it is only able to reconstruct the shape of the objects and needs sufficient amount of independent measured data to guarantee the required performance [1]. Besides, it is very time-consuming to compute the dyadic Green functions related to all the voxels in an irregular inhomogeneous background grid [29].

Inversion techniques have been mainly investigated in cases where the measured data are obtained from a full aperture setup in order to circumvent the occurrence of local minima in the minimization process of the inversion. However, in

many real-life applications, the ROI can only be illuminated within a very limited range of angles. Among the typical applications are the half-space configurations, e.g., GPR imaging [30] and through-the-wall (TW) imaging [31], for which the nonuniqueness is more serious than that of the full aperture cases, because the antennas can only be distributed at a single side of the ROI and only the back-scattered field is available. For solving half-space inverse scattering configurations, the linear focusing methods have been extensively used, e.g., the back-projection method [32], time-reversal (TR) technique [33]–[41], its further variant—TR multiple signal classification (TR MUSIC) [42]–[45], and many more. We refer to [46] for a whole state-of-the-art review. The working principle behind TR imaging is the back propagation of the time-reversed signals observed at the receivers into the imaging region. The process of TR imaging is strictly within the framework of the wave equation, while the back-projection algorithm is a geometrical technique [47], which is not based on the wave equation. It is well known that the imaging resolutions of the linear focusing algorithms are bound by the diffraction limit [48]. In contrast, TR MUSIC became very popular, because it is not only algorithmically efficient but also capable to achieve a resolution that can be much finer than the diffraction limit. As a matter of fact, the method LSM can also be reinterpreted, apart from very peculiar cases, as a synthetic focusing problem [49]. For 2-D quantitative inverse scattering methods based on LSM and CSI, we refer to [50]–[53]. A fast 3-D inversion algorithm for solving inverse problems in layered media has been proposed by Song and Liu using the so-called diagonal tensor approximation. This research has been reported in [54], in which the typical half-space configuration has been discussed. Although this inversion method is efficient, the potential application is limited because of the introduction of an approximate scattering model.

In this paper, a linearized 3-D EM CSI method is proposed and successfully applied to two typical half-space configurations: 1) GPR imaging and 2) TW imaging. Specifically, a finite-difference frequency-domain (FDFD) [55] formulation is used to discretize the forward EM scattering problem, resulting in a highly accurate scattering model, which enables extensive applications to inverse scattering configurations with versatile known backgrounds. With the so-called contrast sources defined as the multiplication of the contrast and the total fields, we can formulate the nonlinear inverse scattering problem into a linear model. To deal with the ill-posedness, the contrast sources are estimated by solving a group of ℓ_1-norm regularized linear problems. A similar idea can be found in the work of Oliveri *et al.* [56], who have proposed a method in which the contrast sources are obtained separately by a Bayesian compressive sensing method, which is, in fact, a single-measurement vector model, because the joint structure of the contrast sources is not considered. In the proposed method, we have exploited the joint structure of the contrast sources by formulating the inverse scattering problem as a linear sum-of-ℓ_1-norm optimization problem with the multiple-measurement vector (MMV) model [57]–[59]. The equivalent problem, referred to as the basis pursuit denoising (BPDN) problem, is solved instead. We refer to [7] for an application

of joint sparsity in the field of medical imaging. As the model is based on an FDFD scheme of the Maxwell equations, it enables simple incorporation of complicated background media. In this paper, a 3-D Cartesian coordinate system is used. Therefore, the contrast at each position is described by three coordinates and, therefore, contains three components. Thus, a group sparse BPDN problem can be obtained, which is solved by a spectral projected gradient for an ℓ_1 minimization (SPGL1) solver [60], [61]. Since the noise level is unknown in real-life applications, a cross-validation (CV) technique [62], [63] is used to check whether the optimization process is sufficient. With the estimated contrast sources, the scattered fields can be computed by solving the corresponding forward EM scattering problems. Assuming that the incident fields are known, the total fields can be easily obtained as the summation of the scattered fields and the incident fields. Finally, the contrast is reconstructed by minimizing a cost functional defined as the sum of the data error and the state error. The contrast is initialized as the least square solution of the state equations, and the range constraints on the real part and the imaginary part of the contrast are considered as *a priori* information.

The proposed method is capable to reconstruct not only the shape but also a coarse estimation of the dielectric parameters of the objects. Since the total fields in the inversion domain are updated only once, this novel method is far more efficient than the traditional iterative inversion methods, e.g., CSI and BIM. We have applied the proposed method to two typical half-space configurations: GPR imaging and TW imaging, and successfully obtained a coarse estimation of the contrast. The forward EM scattering problems are solved by a 3-D FDFD solver "MaxwellFDFD" and its companion C program "FD3D" [64]. Moreover, we have also discussed the performance of the proposed linearized inversion method when the dielectric parameters of the background are not exactly known. The remainder of the paper is organized as follows. In Section II, the formulation of the inverse scattering problem is introduced. In Section III, we introduce the reconstruction of the contrast sources, in which the MMV model, the CV-based modified SPGL1 method, and the construction of the scattering matrix are given. The inversion of the contrast is introduced in Section IV. The inverted results of the numerical experiments of GPR imaging and TW imaging are given in Section V with both exact and inexact background models. Finally, Section VI ends this paper with our conclusions.

II. FORMULATION OF THE INVERSE SCATTERING PROBLEM

We consider a scattering configuration as depicted in Fig. 1, in which sources and receivers are located on the surface $\mathcal{S}$, and the objects are located in the background medium $\mathcal{B} \subset \mathbb{R}^3$. The region $\mathcal{D} \subset \mathcal{B}$ is the imaging domain, which contains the objects. The sources are denoted by the subscript p in which $p \in \{1, 2, 3 \ldots, P\}$, and the receivers are denoted by the subscript q in which $q \in \{1, 2, 3, \ldots, Q\}$. The electric field corresponding to each source is measured by all the receivers. Considering a constant permeability μ_0, we can write the electric field equation in frequency domain based on
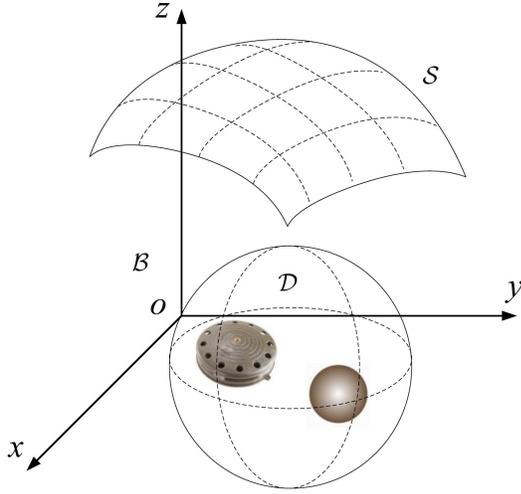
Fig. 1. General geometry of the 3-D inverse scattering problem. Sources and receivers are located on the surface $\mathcal{S}$. Objects are located in the inversion region $\mathcal{D}$.

Maxwell's equations as

$$\nabla \times \mu_0^{-1} \nabla \times \boldsymbol{E}_p - \omega^2 \boldsymbol{\epsilon} \boldsymbol{E}_p = -i\omega \boldsymbol{J}_p^{\text{src}}, \quad p = 1, 2, \ldots, P \tag{1}$$

where $\boldsymbol{E}_p$ and $\boldsymbol{J}_p^{\text{src}}$ are the electric field and the electric current source density corresponding to the source with the index p, respectively; ω is the angular frequency; $\boldsymbol{\epsilon}$ is the complex permittivity given by $\boldsymbol{\epsilon} = \boldsymbol{\varepsilon} - i\boldsymbol{\sigma}/\omega$ with $\boldsymbol{\varepsilon}$ and $\boldsymbol{\sigma}$ representing the permittivity and the conductivity, respectively; i represents the imaginary unit. Note that the time factor is $\exp(i\omega t)$ in this paper. All these quantities are the functions of the position vector $\boldsymbol{x}$ and the angular frequency ω.

Considering the relation of the total fields $\boldsymbol{E}_p^{\text{tot}}$, the incident fields $\boldsymbol{E}_p^{\text{inc}}$, and the scattered fields $\boldsymbol{E}_p^{\text{sct}}$, $\boldsymbol{E}_p^{\text{tot}} = \boldsymbol{E}_p^{\text{sct}} + \boldsymbol{E}_p^{\text{inc}}$, it is easy to obtain the basic equation of the inverse scattering problem, which is denoted by

$$\nabla \times \mu_0^{-1} \nabla \times \boldsymbol{E}_p^{\text{sct}} - \omega^2 \boldsymbol{\epsilon}_b \boldsymbol{E}_p^{\text{sct}} = \omega^2 \boldsymbol{J}_p, \quad p = 1, 2, \ldots, P \tag{2}$$

where $\boldsymbol{J}_p = \boldsymbol{\chi} \boldsymbol{E}_p^{\text{tot}}$ is the contrast source corresponding to the source of the index p. Here, $\boldsymbol{\chi} = \Delta\boldsymbol{\varepsilon} - i\Delta\boldsymbol{\sigma}/\omega$ is the difference of the complex permittivity in the inversion domain with and without the inclusion of the scattering objects and, therefore, is referred to as the contrast. The aim of this paper is to reconstruct the contrast of the scatterers using the back-scattered field probed on the measurement surface $\mathcal{S}$. In the following, we try to fulfill this purpose with measurement data at a single frequency.

III. ESTIMATION OF THE CONTRAST SOURCES

A. Formulation With FDFD

First, the finite-difference scheme is used in the discretization of the 3-D inverse scattering problem. Since we are only interested in a single-frequency inversion, it is advantageous to cast the EM inverse scattering problem into an FDFD scheme. Another advantage is that it is very straightforward to incorporate an inhomogeneous background medium

into this FDFD scheme, resulting in applications of our inversion method to different scenarios with inhomogeneous backgrounds.

Following the vector form of the FDFD scheme in [55], we recast the vectorial equations (2) into the following matrix formalism:

$$\boldsymbol{A} \boldsymbol{e}_p^{\text{sct}} = \omega^2 \boldsymbol{j}_p, \quad p = 1, 2, \ldots, P \tag{3}$$

where $\boldsymbol{A} \in \mathbb{C}^{3N \times 3N}$ is the stiffness matrix in FDFD, which is highly sparse. $\boldsymbol{e}_p^{\text{sct}} \in \mathbb{C}^{3N}$ and $\boldsymbol{j}_p \in \mathbb{C}^{3N}$ are the scattered fields and the contrast sources in the form of a column vector, respectively. Here, N represents the grid number of the discretized 3-D space. Then, the solution to (3) is obtained by inverting the stiffness matrix $\boldsymbol{A}$, which yields

$$\boldsymbol{e}_p^{\text{sct}} = \boldsymbol{A}^{-1} \omega^2 \boldsymbol{j}_p. \tag{4}$$

Considering that the scattered field is measured at a number of positions, we formulate the data equations as follows:

$$\boldsymbol{f}_p = \boldsymbol{M}_p^{\mathcal{S}} \boldsymbol{A}^{-1} \omega^2 \boldsymbol{j}_p, \quad p = 1, 2, \ldots, P \tag{5}$$

where $\boldsymbol{M}_p^{\mathcal{S}}$ is a measurement matrix, selecting the values of the scattered fields at the positions of the receivers. Obviously, this is an under-determined linear system of equations. In order to deal with the ill-posedness, the problem of estimating the contrast sources is regularized by the ℓ_1 norm constraint, which can be formulated as a group of quadratic programming (QP) optimization problems

$$(\text{QP}_{\tilde{\lambda}}) \min_{\boldsymbol{j}_p} \|\boldsymbol{f}_p - \boldsymbol{\Phi}_p \boldsymbol{j}_p\|_2^2 + \tilde{\lambda} \|\boldsymbol{j}_p\|_1$$
$$p = 1, 2, \ldots, P \tag{6}$$

where $\boldsymbol{\Phi}_p = \boldsymbol{M}_p^{\mathcal{S}} \boldsymbol{A}^{-1} \omega^2 \in \mathbb{C}^{M \times 3N}$ is the scattering matrix corresponding to the pth source. An equivalent problem of $(\text{QP}_{\tilde{\lambda}})$—the BPDN problem

$$(\text{BP}_{\tilde{\sigma}}) \min_{\boldsymbol{j}_p} \|\boldsymbol{j}_p\|_1$$
$$\text{s.t. } \|\boldsymbol{f}_p - \boldsymbol{\Phi}_p \boldsymbol{j}_p\|_2 \leq \tilde{\sigma}, \quad p = 1, 2, \ldots, P \tag{7}$$

is solved instead. As a matter of fact, for appropriate parameter choices of $\tilde{\lambda}$ and $\tilde{\sigma}$, the solutions of $(\text{QP}_{\tilde{\lambda}})$ and $(\text{BP}_{\tilde{\sigma}})$ coincide, and the two problems are in some sense equivalent [60]. Since the parameter $\tilde{\sigma}$ is a measure of the noise level, $(\text{BP}_{\tilde{\sigma}})$ is physically more suitable for the inverse scattering problem.

B. Group Sparse BPND: the MMV Model

Although the contrast sources $\boldsymbol{j}_p$ are excited by the illumination of different incident fields $\boldsymbol{e}_p^{\text{inc}}$, the nonzero values are all located on the surfaces and in the interior of the scatterers. Thus, the contrast sources have the same sparse support, which inspired us to enhance the inversion performance by taking advantage of the joint structure [57]. Hence, the $(\text{BP}_{\tilde{\sigma}})$ problem is further formulated as the sum-of-norms optimization problem [61]

$$\min_{\boldsymbol{J}} \sum_{i=1}^{3N} \left\| \boldsymbol{J}_{i,:}^T \right\|_2$$
$$\text{s.t. } \left(\sum_{p=1}^{P} \|\boldsymbol{f}_p - \boldsymbol{\Phi}_p \boldsymbol{j}_p\|_2^2 \right)^{1/2} \leq \tilde{\sigma} \tag{8}$$

where $\boldsymbol{J} = [\boldsymbol{j}_1, \boldsymbol{j}_2, \dots, \boldsymbol{j}_P] \in \mathbb{C}^{3N \times P}$ is a matrix with the contrast sources occupying the columns, and $\boldsymbol{J}_{i,:}^T \in \mathbb{C}^P$ represents the ith row of the matrix $\boldsymbol{J}$. Here, $(\cdot)^T$ represents the transpose operator. An interpretation of the sum-of-norms formulation can be simply stated as finding a matrix $\hat{\boldsymbol{J}}$ which has the least value of the sum of the ℓ_1 norms of the rows while satisfying the inequality.

Considering the 3-D Cartesian coordinate system, the contrast source at one position consists of three components. If the contrast at this position is not zero, then the three components of the corresponding contrast source are very likely to have nonzero values at the same time. Namely, the contrast sources have a group (group of three) sparse structure. Therefore, the problem can be further formulated as a new sum-of-norms optimization problem

$$\min_{\boldsymbol{J}} \ \sum_{k=1}^N \| [\boldsymbol{J}_{3k-2,:} \ \boldsymbol{J}_{3k-1,:} \ \boldsymbol{J}_{3k,:}]^T \|_2$$

$$\text{s.t.} \ \left(\sum_{p=1}^P \| \boldsymbol{f}_p - \boldsymbol{\Phi}_p \boldsymbol{j}_p \|_2^2 \right)^{1/2} \leq \tilde{\sigma} \qquad (9)$$

where $\boldsymbol{J}_{3k-2,:}$, $\boldsymbol{J}_{3k-1,:}$, and $\boldsymbol{J}_{3k,:}$ represent the x-, y-, and z-components of the contrast sources at the position of the index k, respectively. We solve the sum-of-norms optimization problem with the SPGL1 solver [60], [61], of which the basic idea is to find the solution of the BPDN problem by solving a series of Lasso (LS_τ) problems

$$\min_{\boldsymbol{j}_p} \ \left(\sum_{p=1}^P \| \boldsymbol{f}_p - \boldsymbol{\Phi}_p \boldsymbol{j}_p \|_2^2 \right)^{1/2}$$

$$\text{s.t.} \ \sum_{k=1}^N \| [\boldsymbol{J}_{3k-2,:} \ \boldsymbol{J}_{3k-1,:} \ \boldsymbol{J}_{3k,:}]^T \|_2 \leq \tau. \qquad (10)$$

The projection for solving the (LS_τ) problem is implemented by a group projection algorithm (see [61, Th. 6.3]).

C. CV-Based Modified SPGL1

In order to estimate the noise level, i.e., the parameter $\tilde{\sigma}$, the SPGL1 method is modified based on the CV technique [62], [63]. Specifically, we separate the original scattering matrix to a reconstruction matrix $\boldsymbol{\Phi}_{p,r} \in \mathbb{C}^{M_r \times 3N}$ and a CV matrix $\boldsymbol{\Phi}_{p,\text{CV}} \in \mathbb{C}^{M_{\text{CV}} \times 3N}$ with $M = M_r + M_{\text{CV}}$. The measurement vector $\boldsymbol{f}_p$ is also separated accordingly, to a reconstruction measurement vector $\boldsymbol{f}_{p,r} \in \mathbb{C}^{M_r}$ and a CV measurement vector $\boldsymbol{f}_{p,\text{CV}} \in \mathbb{C}^{M_{\text{CV}}}$. The reconstruction residual and the CV residual are defined as

$$\gamma_r := \left(\sum_{p=1}^P \| \boldsymbol{f}_{p,r} - \boldsymbol{\Phi}_{p,r} \boldsymbol{j}_p \|_2^2 \right)^{1/2} \qquad (11a)$$

$$\gamma_{\text{CV}} := \left(\sum_{p=1}^P \| \boldsymbol{f}_{p,\text{CV}} - \boldsymbol{\Phi}_{p,\text{CV}} \boldsymbol{j}_p \|_2^2 \right)^{1/2}. \qquad (11b)$$

In doing so, every iteration can be viewed as two separate parts: 1) reconstructing the contrast sources by SPGL1 and

2) evaluating the outcome by the CV technique, which is used to properly terminate the iteration before the recovery starts to overfit the noise. The reconstructed contrast sources are selected as the output on the criterion that its CV residual is the smallest one.

D. Construction of the Scattering Matrix $\boldsymbol{\Phi}_p$

Note that, as the selecting matrix $\boldsymbol{M}_p^{\mathcal{S}} \in \mathbb{C}^{M \times 3N}$ has a small number of rows, the scattering matrix $\boldsymbol{\Phi}_p$ can be calculated iteratively by solving M linear systems of equations

$$\boldsymbol{A}^T \boldsymbol{\varphi}_{p,m} = \left(\boldsymbol{M}_{p,m}^{\mathcal{S}} \right)^T, \quad m = 1, 2, \dots, M \qquad (12)$$

where $\boldsymbol{M}_{p,m}^{\mathcal{S}}$ is the mth row of the selecting matrix $\boldsymbol{M}_p^{\mathcal{S}}$. $\boldsymbol{\varphi}_m \in \mathbb{C}^{M \times 1}$ constructs the scattering matrix by $\boldsymbol{\Phi}_p = [\boldsymbol{\varphi}_{p,1}, \boldsymbol{\varphi}_{p,2}, \dots, \boldsymbol{\varphi}_{p,M}]^T$. Since M is much smaller than N, the scattering matrix $\boldsymbol{\Phi}_p$ is much smaller compared with the LU matrices of the stiffness matrix $\boldsymbol{A}$ (if we choose to do LU decomposition for fast calculating the inverse of the matrix $\boldsymbol{A}$). This feature makes it possible to compute and store the scattering matrix beforehand, which is of great importance, especially for 3-D inverse scattering problems. It is worth noting that, in the numerical experiments of this paper, the positions of the receivers are fixed for all the measurements, i.e., $\boldsymbol{\Phi}_1 = \boldsymbol{\Phi}_2 = \cdots = \boldsymbol{\Phi}_P$.

IV. INVERSION OF THE CONTRAST

Assuming we have reconstructed the contrast sources, the scattered fields can be estimated by (4). If we know the incident fields, it is easy to obtain the total fields. In order to solve the contrast, we define the data equations and the state equations as follows:

$$\boldsymbol{f}_p = \boldsymbol{\Phi}_p \boldsymbol{D}_{\hat{e}_p^{\text{tot}}} \boldsymbol{\chi}, \quad p = 1, 2, \dots, P \qquad (13a)$$

$$\hat{\boldsymbol{j}}_p = \boldsymbol{D}_{\hat{e}_p^{\text{tot}}} \boldsymbol{\chi}, \quad p = 1, 2, \dots, P. \qquad (13b)$$

The contrast $\boldsymbol{\chi}$ can be obtained by iteratively minimizing the cost functional $\mathcal{C}(\boldsymbol{\chi})$, which is defined as the sum of the data error and the state error

$$\min_{\boldsymbol{\chi}} \mathcal{C}(\boldsymbol{\chi}) := \frac{\| \boldsymbol{f} - \boldsymbol{\Psi} \boldsymbol{\chi} \|_2^2}{\| \boldsymbol{f} \|_2^2} + \frac{\| \hat{\boldsymbol{j}} - \boldsymbol{D}_{\hat{e}_p^{\text{tot}}} \boldsymbol{\chi} \|_2^2}{\| \boldsymbol{D}_{\hat{e}_p^{\text{inc}}} \boldsymbol{\chi} \|_2^2} \qquad (14)$$

where

$$\boldsymbol{f} = \begin{bmatrix} \boldsymbol{f}_1^T & \boldsymbol{f}_2^T & \dots & \boldsymbol{f}_P^T \end{bmatrix}^T \qquad (15)$$

$$\boldsymbol{j} = \begin{bmatrix} \boldsymbol{j}_1^T & \boldsymbol{j}_2^T & \dots & \boldsymbol{j}_P^T \end{bmatrix}^T \qquad (16)$$

$$\boldsymbol{D}_{\hat{e}_p^{\text{tot}}} = \text{diag}\{\boldsymbol{e}_p^{\text{tot}}\}, \quad p = 1, 2, \dots, P \qquad (17)$$

$$\boldsymbol{D}_{\hat{e}_p^{\text{inc}}} = \text{diag}\{\boldsymbol{e}_p^{\text{inc}}\}, \quad p = 1, 2, \dots, P \qquad (18)$$

and

$$\boldsymbol{\Psi} = \begin{bmatrix} \boldsymbol{\Phi}_1 \boldsymbol{D}_{\hat{e}_1^{\text{tot}}} \\ \boldsymbol{\Phi}_2 \boldsymbol{D}_{\hat{e}_2^{\text{tot}}} \\ \vdots \\ \boldsymbol{\Phi}_P \boldsymbol{D}_{\hat{e}_P^{\text{tot}}} \end{bmatrix}. \qquad (19)$$

Specifically, χ is updated through

$$\chi_n = \chi_{n-1} + \alpha_n \boldsymbol{v}_{\chi,n} \tag{20}$$

where α_n is a constant and the update direction $\boldsymbol{v}_{\chi,n}$ is chosen to be the Polak–Ribière conjugate gradient directions given by

$$\boldsymbol{v}_{\chi,0} = 0$$
$$\boldsymbol{v}_{\chi,n} = \boldsymbol{g}_{\chi,n} + \frac{\langle \boldsymbol{g}_{\chi,n}, \boldsymbol{g}_{\chi,n} - \boldsymbol{g}_{\chi,n-1} \rangle_2}{\|\boldsymbol{g}_{\chi,n-1}\|_2^2} \boldsymbol{v}_{\chi,n-1} \ n \geq 1 \tag{21}$$

where, $\boldsymbol{g}_{\chi,n}$ is the gradient of the contrast cost functional $\mathcal{C}(\chi)$ given by

$$\boldsymbol{g}_{\chi,n} = \frac{-2\boldsymbol{\Psi}^H(\boldsymbol{f} - \boldsymbol{\Psi}\chi_{n-1})}{\|\boldsymbol{f}\|_2^2} + \frac{-2\boldsymbol{D}_{\hat{e}_p^{\text{tot}}}^H(\hat{\boldsymbol{j}} - \boldsymbol{D}_{\hat{e}_p^{\text{tot}}}\chi_{n-1})}{\left\|\boldsymbol{D}_{\hat{e}_p^{\text{inc}}}\chi_{n-1}\right\|_2^2}. \tag{22}$$

Here, $\langle \cdot, \cdot \rangle_2$ represents the inner product of two vectors, and $(\cdot)^H$ represents the conjugate transpose of a matrix. The step size α_n is determined by minimizing the cost function as follows:

$$\mathcal{C}_n(\alpha_n) = \frac{\|\boldsymbol{f} - \boldsymbol{\Psi}(\chi_{n-1} + \alpha_n \boldsymbol{v}_{\chi,n})\|_2^2}{\|\boldsymbol{f}\|_2^2} + \frac{\left\|\hat{\boldsymbol{j}} - \boldsymbol{D}_{\hat{e}_p^{\text{tot}}}(\chi_{n-1} + \alpha_n \boldsymbol{v}_{\chi,n})\right\|_2^2}{\left\|\boldsymbol{D}_{\hat{e}_p^{\text{inc}}}(\chi_{n-1} + \alpha_n \boldsymbol{v}_{\chi,n})\right\|_2^2} \tag{23}$$

which is a problem of finding the minimum of a single-variable function, and can be efficiently solved using Brent's method [65], [66].

The contrast is initialized using the least square solution to the state equations (13b), that is

$$\chi_0 = \left(\boldsymbol{D}_{\hat{e}_p^{\text{tot}}}\boldsymbol{j}\right) \oslash \left(\boldsymbol{D}_{\hat{e}_p^{\text{tot}}}\overline{\hat{e}_p^{\text{tot}}}\right) \tag{24}$$

where $\oslash$ represents the element-wise division.

By considering the relation $\boldsymbol{\epsilon} = \boldsymbol{\epsilon} - \boldsymbol{\epsilon}_b$, where $\boldsymbol{\epsilon}$ and $\boldsymbol{\epsilon}_b$ are the complex permittivities of the test domain and the background, and noting the fact that

$$\Re\{\boldsymbol{\epsilon}\} \succeq 1, \quad \Im\{\boldsymbol{\epsilon}\} \preceq 0 \tag{25}$$

we can simply obtain

$$\Re\{\boldsymbol{\chi}\} \succeq 1 - \Re\{\boldsymbol{\epsilon}_b\}, \quad \Im\{\boldsymbol{\chi}\} \preceq -\Im\{\boldsymbol{\epsilon}_b\}. \tag{26}$$

Here, $\Re\{\cdot\}$ and $\Im\{\cdot\}$ represent the real part and the imaginary part of a number or a vector; $\succeq$ and $\preceq$ represent the component-wise inequality between the elements of a vector and a constant. Therefore, range constraints are considered in the iterations as *a priori* information, which is done by setting the real part to $1 - \Re\{\boldsymbol{\epsilon}_b\}$ whenever $\Re\{\boldsymbol{\chi}_n\} < 1 - \Re\{\boldsymbol{\epsilon}_b\}$, and setting the imaginary part to $-\Im\{\boldsymbol{\epsilon}_b\}$ whenever $\Im\{\boldsymbol{\chi}_n\} > -\Im\{\boldsymbol{\epsilon}_b\}$. In our experiments, the contrast is assumed to be isotropic, i.e., $\chi_{3k-2} = \chi_{3k-1} = \chi_{3k}$. Therefore, we use the mean of the three components as the final estimation of the contrast.

V. NUMERICAL EXPERIMENTS

A. Configuration

In this section, the proposed linearized 3-D CSI method is applied to two typical 3-D half-space inverse problems: 1) GPR imaging and 2) TW imaging. The forward EM scattering problem is solved by a MATLAB-based 3-D FDFD package "MaxwellFDFD" and its companion C program "FD3-D" [64]. Considering a 3-D Cartesian coordinate system, the x-, y-, and z-normal boundaries of a rectangular region are covered by perfect matching layers (PML) to simulate the anechoic chamber environment. Nonuniform meshes are used to generate the scattered data, which means the testing domain is discretized with different mesh sizes according to the distribution of the permittivity, viz., coarse meshes for low permittivity and fine meshes for high permittivity. The accuracy of the FDFD scheme is ensured by the following criterion [55]:

$$\Delta \leq \frac{\lambda_0}{15\sqrt{\varepsilon_r}} \tag{27}$$

where λ_0 is the wavelength in free space and ε_r is the relative permittivity of the testing domain. Nonuniform meshes greatly reduce the computational burden for solving the forward scattering problem. In contrast, uniform meshes are used to invert the scattered data, since the distribution of the permittivity is unknown beforehand. In order to guarantee the inverting accuracy, we make sure that the following condition is satisfied:

$$\Delta \leq \frac{\lambda_0}{15\sqrt{\max\{\varepsilon_r\}}}. \tag{28}$$

The source used in the numerical experiments consists of an x-polarized electric dipole and a y-polarized one. A circular polarized wave is generated at 200 MHz by introducing a $\pi/2$ phase shift between the two dipoles. The x- and y-components of the electric fields are measured at several positions simultaneously. For the two half-space configurations, 6×6 sources are uniformly distributed on the xoy plane $([-3, 3], [-3, 3], z)$ m, and 9×9 receivers are uniformly distributed in the same region. The distance between the receivers both along the x- and y-axes is $\lambda_0/2 = 0.75$ m. Here, λ_0 is the wavelength of the generated wave in free space.

The measurement data used for inversion consist of the scattered fields obtained by subtracting the incident fields from the probed total fields. Random white noise is added to the measurement data following the similar procedure in [67]:

$$\boldsymbol{f}_{p,\text{noise}} = \boldsymbol{f}_p + \zeta \times \max_m\{|f_{p,m}|\}(\boldsymbol{n}_1 + i\boldsymbol{n}_2)$$
$$p = 1, 2, \ldots, P, \quad m = 1, 2, \ldots, M \tag{29}$$

where $\boldsymbol{n}_1$ and $\boldsymbol{n}_2$ are two random numbers varying from -1 to 1, ζ represents the amount of noise, and $\max_m\{|f_{p,m}|\}$ represents the largest value among the amplitudes of the M measurement data, which means the noise is scaled by the largest amplitude of the measurement data. In the following examples, the measurement data are disturbed according to (29) with $\zeta = 0.05$.
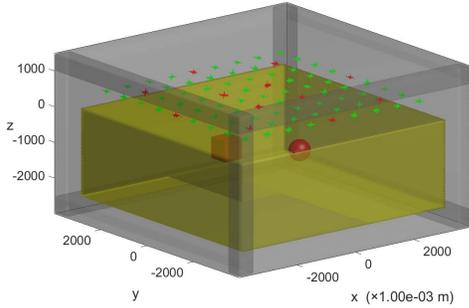
Fig. 2. Geometry of the GPR imaging experiment. Soil: $\epsilon_r = 3$ and $\sigma = 0.001$ S/m. Sphere: $\epsilon_r = 2$ and $\sigma = 0.05$ S/m. Cube: $\epsilon_r = 6$ and $\sigma = 0.01$ S/m. The 6×6 sources and 9×9 receivers are uniformly distributed on the square plane $([-3, 3], [-3, 3], 0.5)$ m. Twelve red receivers: CV measurements. Sixty-nine green receivers: measurements used for reconstructing the contrast sources.

B. GPR Imaging: Lossy Objects

In this section, we consider the inversion of two lossy objects, a sphere ($\varepsilon_r = 2$ and $\sigma = 0.05$ S/m) of radius 0.3 m and a cube ($\varepsilon_r = 6$ and $\sigma = 0.01$ S/m) of side length 0.6 m, buried in lossy soil ($\varepsilon_r = 3$ and $\sigma = 0.001$ S/m). The testing domain is $([-3.5, 3.5], [-3.5, 3.5], [-2.5, 1])$ m. The sources and receivers are uniformly located on the square plane $([-3, 3], [-3, 3], 0.5)$ m, and the half space $-2.5 \ m < z < 0 \ m$ is filled with soil. The sphere is centerd at $([0.7, -0.7, -1])$ m, and the cube is in the region $([-1, -0.4], [0.4, 1], [-1.3, -0.7])$ m. Fig. 2 shows the geometry of this experiment, in which the 9×9 receivers are shown with different colors—69 receivers in green color and 12 receivers in red color. The green ones represent the reconstruction measurements and the red ones represent the CV measurements in the optimization process of estimating the contrast sources.

For creating the scattering matrix $\boldsymbol{\Phi}_p$, we discretize the test domain with uniform mesh resolution determined by (28), and assemble $\boldsymbol{\Phi}$ with the vectors $\boldsymbol{\varphi}_m$ obtained by solving the M linear system of equations (12). In order to decrease the computational burden, we constrain the inversion domain in the region $([-2, 2], [-2, 2], [-2.5, 0])$ m. As a matter of fact, more meshes are used due to the introduction of the PMLs. In our simulations, iterative solvers are used in solving the 3-D forward scattering problems and the scattering matrix. The computation was accelerated by parallel computing programming with 16 cores.

Fig. 3(a) shows the reconstruction residual and the CV residual in the iterative process of estimating the contrast sources, from which we can see that the reconstruction residual curve and the CV residual curve have a stair-like shape. As a matter of fact, the ith stair corresponds to the (LS_τ) problem with the parameter τ_i. See [60] for more details about the updating criterion of the parameter τ. From the subview shown in Fig. 3(a), we can see that the CV residual starts to increase at the 179th iteration, while the reconstruction residual can still be minimized further. This indicates that the iteration process starts to overfit the noise. Therefore, the contrast sources are supposed to be chosen as the approximate solution that corresponds to the smallest CV residual. Fig. 3(b) shows the
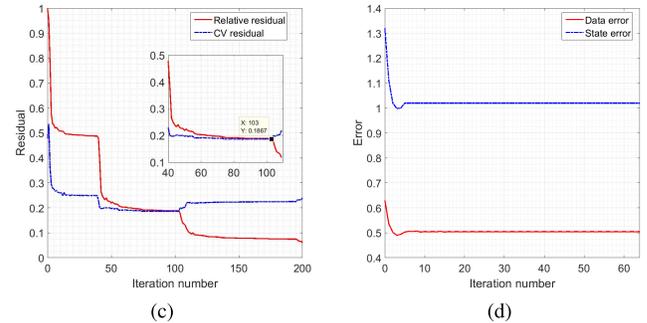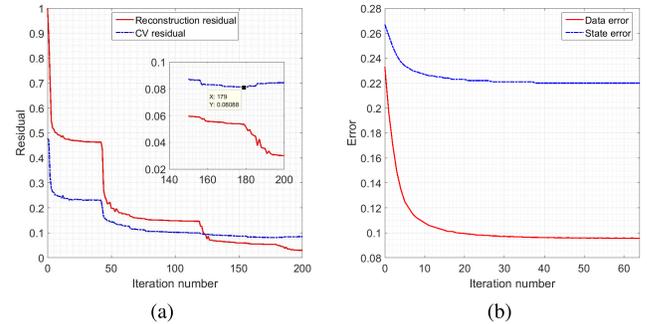
Fig. 3. Residual curves of the GPR imaging experiment. (a) and (c) Reconstruction residual and CV residual curves for estimating the contrast sources using exact background model and inexact background model $(1.25\epsilon_b)$, respectively. (b) and (d) Data error and state error curves for reconstructing of the contrast using exact background model and inexact background model $(1.25\epsilon_b)$, respectively.

data error curve and the state error curve. From Fig. 3(b), we can see a relatively large state error 22% has been preserved and cannot be minimized after 40 iterations due to the inexact estimation of the contrast sources, while, in this experiment, the data error has been minimized to a relatively small one 9%.

The shape of the reconstructed results is shown in Fig. 4. Since the contrast is assumed to be isotropic, the shape of the original contrast is defined as

$$I_k = \left| \frac{\chi_{3k-2} + \chi_{3k-1} + \chi_{3k}}{3} \right|, \quad k = 1, 2, \ldots, N \quad (30)$$

and is shown in Fig. 4(a). The shape of the contrast sources is defined as

$$I_k = \sum_{p=1}^{P} \sqrt{|\boldsymbol{j}_{p,3k-2}|^2 + |\boldsymbol{j}_{p,3k-1}|^2 + |\boldsymbol{j}_{p,3k}|^2}$$
$$k = 1, 2, \ldots, N \quad (31)$$

and is shown in Fig. 4(b), from which we can see that the contrast sources are elongated along the z-axis, indicating good resolution along the x- and y-axes and poor resolution along the z-axis. This can be explained by the planar distribution of the sources and the receivers. Due to the limited aperture in the half-space configurations, the nonuniqueness of the inverse problem gets worse. As a result, it is extremely difficult to do exact reconstruction. Fig. 4(c) and (d) shows the shape of the reconstructed contrast permittivity and the reconstructed contrast conductivity, from which we can see that the location and the basic shape of the buried objects can be well reconstructed.
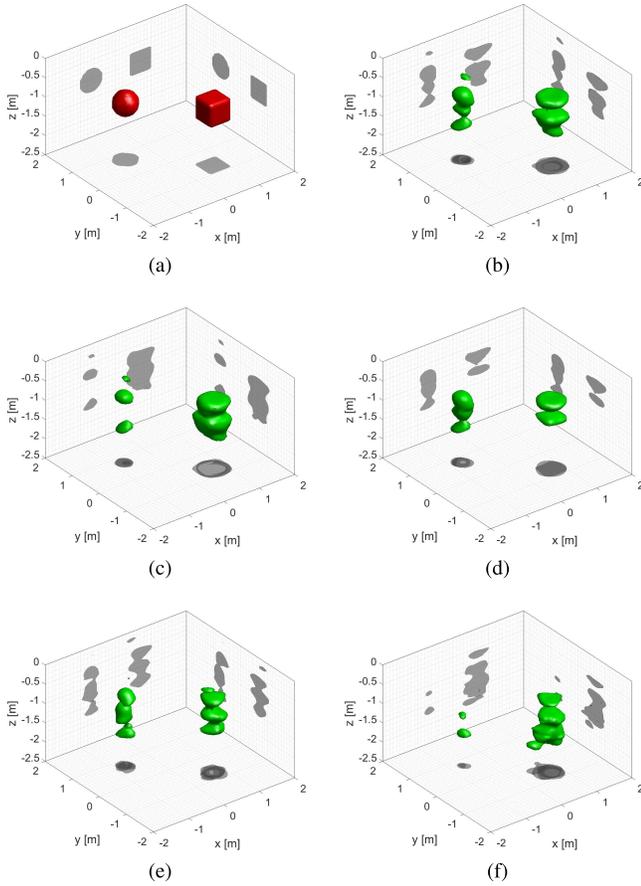
Fig. 4. Three-dimensional shape of the reconstructed results in the GPR imaging experiment at 200 MHz. 5% random white noise is added. (a) True objects. (b) Reconstructed contrast sources. (c) and (d) Reconstructed contrast permittivity and conductivity using exact background model. (e) and (f) Reconstructed contrast permittivity and conductivity using inexact background model ($1.25\epsilon_b$).

Fig. 5. Cross sections of the reconstructed dielectric parameters in the GPR imaging experiment at 200 MHz. 5% random white noise is added. The unit of the conductivity is S/m. (a) True contrast permittivity. (b) True contrast conductivity. (c) and (d) Reconstructed contrast permittivity and conductivity using exact background model. (e) and (f) Reconstructed contrast permittivity and conductivity using inexact background model ($1.25\epsilon_b$).

To study the estimation accuracy of the dielectric parameters, Fig. 5 shows the cross sections ($x = 0.7$ m, $y = 0.7$ m, and $z = -1.15$ m) of the reconstructed contrast permittivity and conductivity, together with those of the real ones. By comparing Fig. 5(a) and (c), we see that the reconstructed contrast permittivity has negative values down to -1.7 (the real one is -2) in the top region of the sphere, while the one for the cube has positive values up to 2.4 (the real one is 3). Although the estimation of the dielectric parameters is not very accurate, it well consists with the real situation. From Fig. 5(b), we can see that the sphere has larger conductivity than the cube, this is well presented in the reconstructed results shown in Fig. 5(d), and the maximum value of the estimated contrast conductivity is 0.04 S/m, which is very close to the real value of 0.05 S/m.

In order to study the influence of the background mismatch to the inversion performance of the proposed method, we process the same measurement data with an inexact background model. Specifically, we assume that the geometry of the ground is exactly known, but the dielectric parameters of the soil are estimated higher than the exact value by 25%. It is worth noting that the incident fields, as well as the scattering matrix Φ_p, have to be recalculated according to the inexact background model. In addition, the contrast must be restricted

according to the newly estimated dielectric parameters of the soil. Fig. 4(e) and (f) shows the shape of the inverted results obtained by processing the same measurement data with the inexact dielectric parameters of the soil ($1.25 \times \epsilon_b$). From Fig. 4(e) and (f), we can see that more artefacts have been reconstructed due to the mismatch of the background model. The resolution in the x- and y-dimensions is still acceptable, but the resolution in the z-dimension gets worse. Fig. 5(e) and (f) shows the cross sections ($x = 0.7$ m, $y = 0.7$ m, and $z = -1.15$ m) of the reconstructed contrast permittivity and conductivity, from which we can see that the mismatch seriously degrades the reconstruction accuracy about the dielectric parameters of the objects.

C. TW Imaging

In this section, we consider the inversion of a cross object placed behind a wall ($\varepsilon_r = 4$ and $\sigma = 0.01$ S/m). The testing domain is $([-3.5, 3.5], [-3.5, 3.5], [-3, 1.5])$ m. The 6×6 sources and the 9×9 receivers are uniformly located on the square plane $([-3, 3], [-3, 3], 1)$ m, and the wall is in the region $([-3.5, 3.5], [-3.5, 3.5], [0, 0.5])$ m. The cross object is combined with two rectangular blocks in the regions $([-1, 1], [-0.25, 0.25], [-1.5, -1])$ m and $([-0.25, 0.25], [-1, 1], [-1.5, -1])$ m. The geometry of the TW imaging experiment is shown in Fig. 6. The receivers are shown with different colors, of which the green ones represent
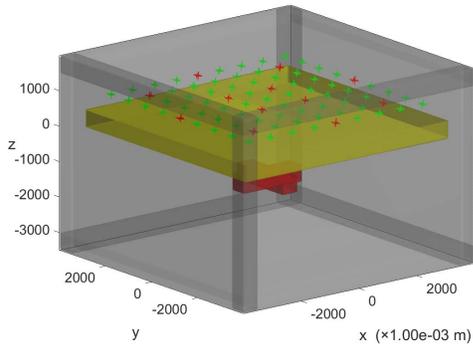
Fig. 6. Geometry of the TW imaging experiment. Wall: $\epsilon_r = 4$ and $\sigma = 0.01$ S/m. Object: lossy material $\epsilon_r = 2$ and $\sigma = 0.001$ S/m, and highly conductive material $\epsilon_r = 1$ and $\sigma = 1$ S/m. The wall is in the region ($[-3.5, 3.5]$, $[-3.5, 3.5]$, $[0, 0.5]$) m. The 6×6 sources and 9×9 receivers are uniformly distributed on the square plane ($[-3, 3]$, $[-3, 3]$, 1) m. Twelve red dots: CV measurements. Sixty-nine green dots: reconstruction measurements.
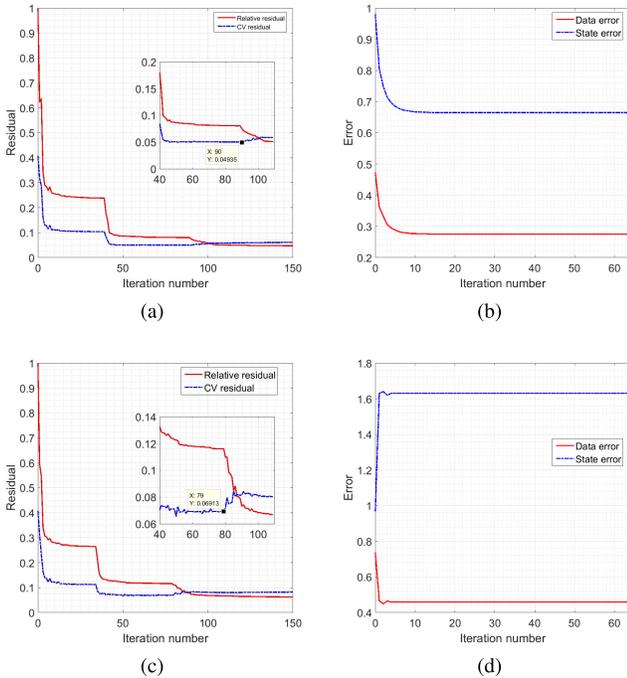
Fig. 7. Residual curves of the TW imaging experiment with lossy object. (a) and (c) Reconstruction residual and CV residual curves for estimating the contrast sources using exact background model and inexact background model ($0.75\epsilon_b$), respectively. (b) and (d) Data error and state error curves for reconstructing the contrast using exact background model and inexact background model ($0.75\epsilon_b$), respectively.

the reconstruction measurements and the red ones represent the CV measurements. The inversion domain is constrained in the region ($[-2, 2]$, $[-2, 2]$, $[-2.5, 0]$) m.

In this TW imaging experiment, we investigate the inversion performance of the proposed method not only to the lossy object but also to the highly conductive object. For the latter, the morphological information is of more interest. The exact and inexact wall models are all considered for solving the scattering matrix $\mathbf{\Phi}_p$ and modeling the incident fields.

1) Lossy Object: Let us first use the lossy cross object whose relative permittivity $\varepsilon_r = 2$ and conductivity $\sigma = 0.001$ S/m. The TW measurement data were disturbed by 5% random white noise according to (29), and were then
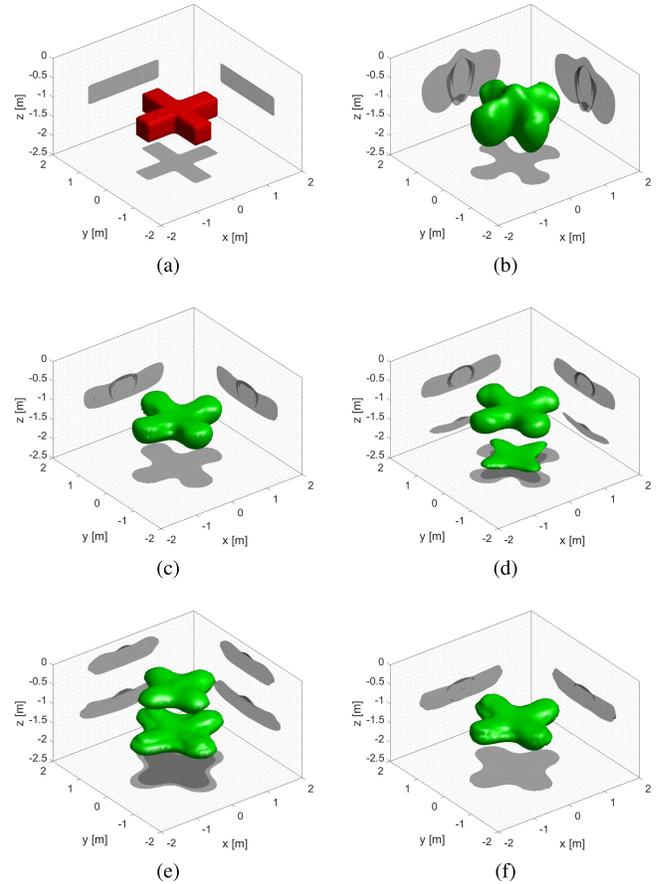
Fig. 8. Three-dimensional shape of the reconstructed results in the TW imaging experiment at 200 MHz. 5% random white noise is added. (a) True objects. (b) Reconstructed contrast sources. (c) and (d) Reconstructed contrast permittivity and conductivity using exact background model. (e) and (f) Reconstructed contrast permittivity and conductivity using inexact background model ($0.75\epsilon_b$).

inverted with the incident fields and the scattering matrix calculated with the exact wall model. Fig. 7(a) shows the reconstruction residual curve and the CV residual curve for recovering the contrast sources. The CV residual reaches the smallest at the iteration 90, where we obtain the optimal solution of the contrast sources. Fig. 7(b) shows the data error curve and the state error curve for reconstructing the contrast. The iterative process converges after ten iterations; however, there is a relatively large data error of 0.27 and a state error of 0.67 that cannot be minimized any more. This is due to the inexact estimation of the contrast sources, which can be obviously seen from Fig. 8(a) and (b), in which the shape of the real object and the reconstructed contrast sources are shown.

As a matter of fact, a good inversion can hardly be achieved with just the back-scattered fields due to the limited amount of independent measurement data. In our method, the contrast sources and the total fields are fixed while reconstructing the contrast, such that the iterative process can be prevented from converging to a local optimal solution which might be far away from the real solution. Fig. 8(c) and (d) shows the shape of the reconstructed contrast permittivity and the reconstructed contrast conductivity, and the corresponding
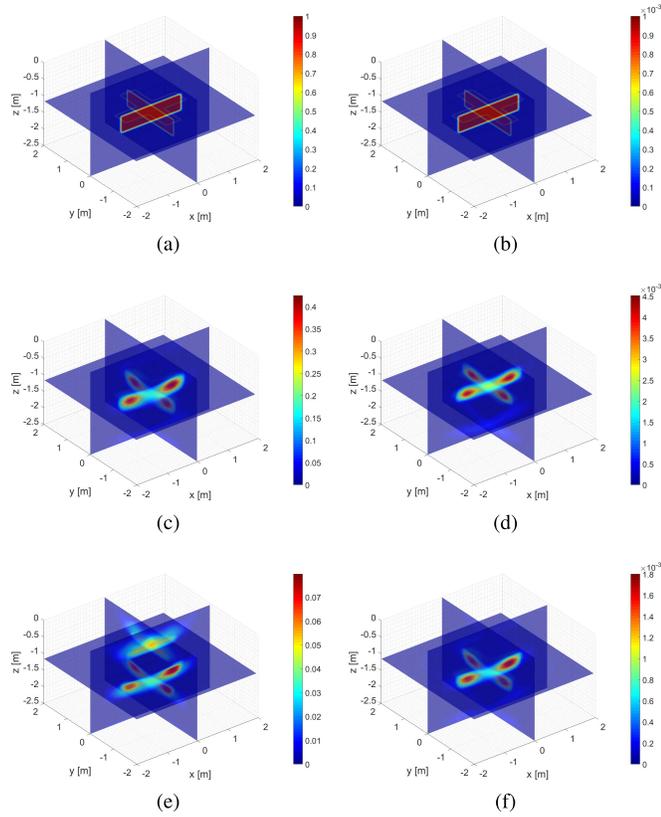
Fig. 9. Cross sections of the reconstructed dielectric parameters in the TW imaging experiment at 200 MHz. 5% random white noise is added. The unit of the contrast conductivity is S/m. (a) True contrast permittivity. (b) True contrast conductivity. (c) and (d) Reconstructed contrast permittivity and conductivity using exact background model. (e) and (f) Reconstructed contrast permittivity and conductivity using inexact background model ($0.75\epsilon_b$).

Fig. 10. Residual curves of the TW imaging experiment with highly conductive object. (a) and (c) Reconstruction residual and CV residual curves for estimating the contrast sources using exact background model and inexact background model (the thickness is 0.75 m), respectively. (b) and (d) Data error and state error curves for reconstructing the contrast using exact background model and inexact background model (the thickness is 0.75 m), respectively.

cross sections ($x = 0$ m, $y = 0$ m, and $z = -1.15$ m) are shown in Fig. 9(c) and (d). For better comparison, the cross sections of the exact parameters are also shown in Fig. 9(a) and (b). We can see from Fig. 8(a), (c), and (d) that the shape of the cross is nicely reconstructed. The shown artefact in the reconstructed contrast conductivity is actually very weak compared with the reconstructed object, which can be seen from Fig. 9(d). If we average the reconstructed parameters in the cross region, then we have a coarse estimation of the contrast $\Delta\hat{\varepsilon}_r \approx 0.2$ and $\Delta\hat{\sigma} \approx 0.002$ S/m.

Assume that the dielectric parameters of the wall are underestimated by 25%, the incident fields and the scattering matrix have to be recalculated correspondingly. However, since the object is surrounded by free space, the range constraints given by (26) keep the same. We do inversion to the same disturbed measurement data. Fig. 7(c) shows the reconstruction residual curve and the CV residual curve for recovering the contrast sources, and Fig. 7(d) shows the data error curve and the state error curve for reconstructing the contrast. The CV residual starts to increase at the iteration 79, where we obtain the optimal solution of the contrast sources. By the comparison of Fig. 7(b) and (d), we can see that the inexact wall model results in larger data error (0.45) and state error (1.65) compared with the one with the exact background model. The shape of the reconstructed contrast permittivity and the contrast conductiv-

ity with inexact wall model are shown in Fig. 8(e) and (f), respectively. In addition, the corresponding cross sections are given in Fig. 9(e) and (f). An obvious ghost cross above the real object can be seen in the reconstructed contrast permittivity, while the reconstructed contrast conductivity is still good enough to identify the object. By the comparison of Fig. 9(c) and (d) and (e) and (f), we see that, after introducing the mismatch of the background, the reconstructed contrast conductivity stays at the same order of magnitude, while the reconstructed contrast conductivity is lower than the exact value of 1 by around one order of magnitude.

2) Highly Conductive Object: To study the performance of the proposed method for the inversion of highly conductive objects, let us now test a cross object of the same size but made of highly conductive material ($\varepsilon_r = 1$ and $\sigma = 10^5$ S/m). First, let us process the measurement data using the exact background model. Namely, we do the same thing as that of the previous lossy cross object, but only replacing the measurement data. Fig. 10(a) and (b) shows the residual curves of recovering both the contrast sources and the contrast. We can see that the data error and the state error are larger than those of inverting the lossy cross object, indicating that the contrast sources are reconstructed with a larger error. Fig. 11(a) and (b) shows the shape of real cross object and the shape of the inverted contrast sources, from which we can see that the contrast sources have a basic cross-like shape extending along the z-axis from $z_1 = -0.5$ m to $z_2 = -1.5$ m. As a matter of fact, for highly conductive
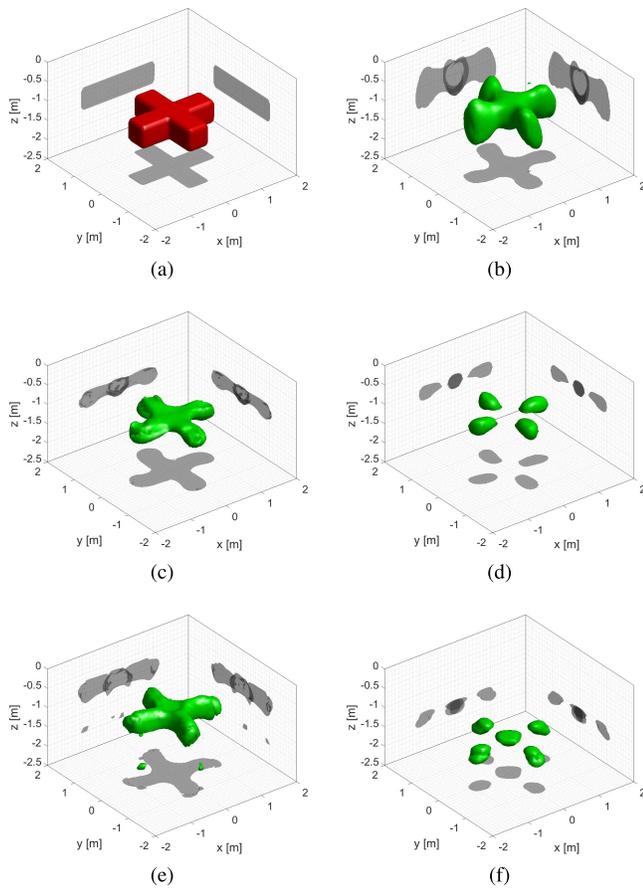
Fig. 11.   Three-dimensional shape of the reconstructed results in the TW imaging experiment at 200 MHz. 5% random white noise is added. (a) Real objects. (b) Reconstructed contrast sources. (c) and (d) Reconstructed contrast permittivity and conductivity using exact background model. (e) and (f) Reconstructed contrast permittivity and conductivity using inexact background model (the thickness is 0.75 m).

Fig. 12.   Cross sections of the reconstructed dielectric parameters in the TW imaging experiment at 200 MHz. 5% random white noise is added. The unit of the contrast conductivity is S/m. (a) True contrast permittivity. (b) True contrast conductivity. (c) and (d) Reconstructed contrast permittivity and conductivity using exact background model. (e) and (f) Reconstructed contrast permittivity and conductivity using inexact background model (the thickness is 0.75 m).

objects, the contrast sources are supposed to distribute on the top surface of the object, and the EM fields in the interior are 0 due to the serious attenuation. This nicely explains why the middle of the contrast sources is exactly the top surface of the real object, i.e., $(z_1 + z_2)/2 = -1$ m. The reconstructed contrast permittivity and the contrast conductivity are shown in Fig. 11(c) and (d), and the corresponding cross sections are shown in Fig. 12(c) and (d). We can see that a ghost of the contrast permittivity is reconstructed with a maximum value of 1, and the reconstructed contrast conductivity is more focused on the top surface of the cross object due to the higher conductivity compared with the lossy cross object. Although the estimation of the dielectric parameters is not accurate in the inversion of highly conductive objects, we get the basic morphological information of the object in the inverted results, which is of more importance in real-life applications.

In the inversion with inexact wall model, we changed the thickness of the wall to 0.75 m while using the exact dielectric parameters. The residual curves are shown in Fig. 10(c) and (d). Obviously, the data error and the state error are larger than those of the inversion using the exact wall model [see Fig. 10(a) and (b)]. The corresponding inverted
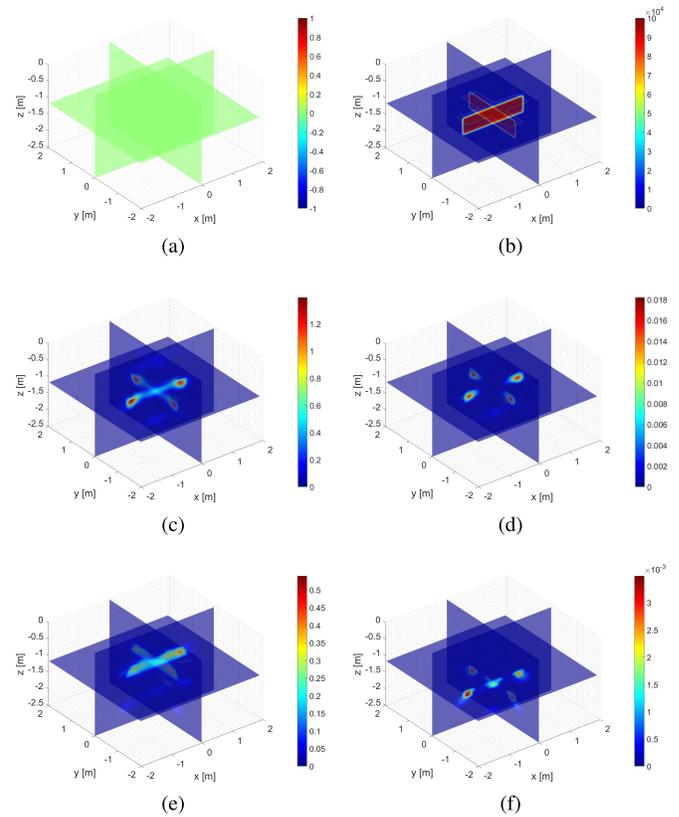
results are shown in Figs. 11(e) and (f) and 12(e) and (f), from which we can see that the contrast permittivity is lifted up by 0.25 m, and the contrast conductivity is lowered by 0.5 m. This is a very interesting phenomenon, because the mismatch of the background model is reflected by the mismatch of the contrast permittivity and the contrast conductivity.

D. Numerical Performance

To summarize this section, we remark that the linearized 3-D inversion method gives good inverted results for the inversion of lossy objects in GPR imaging and TW imaging. It is also able to provide the morphological information of highly conductive objects. The quality of the estimation of the background is critical for ensuring the accuracy of the inverted results. This method leaves a large data error and a large state error for solving the 3-D half-space inverse problems. However it helps to prevent the iterative process from converging to a totally false local optimal solution in the cases where only back-scattered fields are available.

In the numerical experiments, the codes for reconstructing the contrast sources and the contrast are written by MATLAB codes. We ran the codes on a desktop with one Intel(R) Core(TM) i5-3470 CPU at 3.2 GHz, and we did not use parallel computing. The running time of each iteration is

3.1 and 2 s, respectively, for the GPR case, and 3.5 and 2.2 s, respectively, for the TW case. The codes of solving the total fields are written with "C" language and PETSc. We ran the codes on a server with two Intel(R) Xeon(R) CPUs E5-2650 v2 at 2.6 GHz containing 16 cores totally. Parallel computing was used with 16 cores. The running time of solving the total field for each source is 48 s for the GPR case and 25 s for the TW case. In the GPR case, we ran 200 iterations for recovering the contrast sources and 20 iterations for recovering the contrast, and the total running time is $\sim$40 min $[(200 \times 3.1 + 20 \times 2 + 36 \times 48)/60]$. In the TW case, we ran 150 iterations for recovering the contrast sources and 20 iterations for recovering the contrast, and the total running time is $\sim$27.4 min $[(150 \times 3.5 + 20 \times 2.2 + 36 \times 25)/60]$. However, if we implement the MATLAB codes using parallel computing technique with 16 cores, the running time can be reduced by at least eight times. In doing so, the total running time can be further reduced to 30 and 16.5 min, respectively. While for the traditional iterative inversion methods, such as CSI and BIM, the update of the total fields in each iteration requires at least about 57.6 min $[(2 \times 36 \times 48)/60]$ and about 30 min $[(2 \times 36 \times 25)/60]$, respectively. The total running times are at least a multiple of the above times, where the multiple is determined by the required iteration number. This shows that the proposed method is far more efficient in comparison with the traditional iterative inversion methods.

VI. Conclusion

In this paper, we have proposed to exploit the joint structure of the contrast sources in order to overcome the ill-posedness of the inverse scattering problem. The contrast sources are obtained by solving a linear sum-of-ℓ_1-norm optimization problem, of which the objective is to obtain a regularized solution, instead of finding the sparsest solution. The inversion domain is discretized for the application of an FDFD scheme to model the EM state equation in the scattering problem, resulting in a highly accurate scattering model, which can be applied to configurations with a versatile known background. In the case where the scattering objects extending over a large region, the influence of the regularization constraint becomes less significant. However, this problem can be, to a very large extent, overcome by a multifrequency version of the proposed method, which is going to be discussed in another paper. With the estimated contrast sources, a linearized 3-D EM contrast source inversion method is further proposed. The proposed method is tested successfully in a GPR configuration and a TW configuration together with a 3-D FDFD solver. The inversion quality with both exact and inexact background models is discussed, and its sensitivity of the reconstruction in relation to the background medium estimation is shown. The results show that this method is not only efficient but also robust with respect to the reconstruction quality when the acquired measured data from a one side illumination is limited. In the following work, we will apply the proposed method to GPR and TW configurations using real measured data.

References

[1] D. Colton and R. Kress, *Inverse Acoustic and Electromagnetic Scattering Theory*, vol. 93. New York, NY, USA: Springer, 2013.

[2] S. Kuroda, M. Takeuchi, and H. J. Kim, "Full-waveform inversion algorithm for interpreting crosshole radar data: A theoretical approach," *Geosci. J.*, vol. 11, no. 3, pp. 211–217, 2007.

[3] J. R. Ernst, H. Maurer, A. G. Green, and K. Holliger, "Full-waveform inversion of crosshole radar data based on 2-D finite-difference time-domain solutions of Maxwell's equations," *IEEE Trans. Geosci. Remote Sens.*, vol. 45, no. 9, pp. 2807–2828, Sep. 2007.

[4] J. Virieux and S. Operto, "An overview of full-waveform inversion in exploration geophysics," *Geophysics*, vol. 74, no. 6, pp. WCC1–WCC26, 2009.

[5] N. Bleistein *et al.*, *Mathematics of Multidimensional Seismic Imaging, Migration, and Inversion*, vol. 13. New York, NY, USA: Springer, 2013.

[6] C. Gilmore, A. Abubakar, W. Hu, T. M. Habashy, and P. M. van den Berg, "Microwave biomedical data inversion using the finite-difference contrast source inversion method," *IEEE Trans. Antennas Propag.*, vol. 57, no. 5, pp. 1528–1538, May 2009.

[7] O. Lee, J. M. Kim, Y. Bresler, and J. C. Ye, "Compressive diffuse optical tomography: Noniterative exact reconstruction using joint sparsity," *IEEE Trans. Med. Imag.*, vol. 30, no. 5, pp. 1129–1142, May 2011.

[8] A. Rosenthal, V. Ntziachristos, and D. Razansky, "Acoustic inversion in optoacoustic tomography: A review," *Current Med. Imag. Rev.*, vol. 9, no. 4, pp. 318–336, 2013.

[9] J. Hadamard, *Lectures on Cauchy's Problem in Linear Partial Differential Equations*. Mineola, NY, USA: Dover, 2014.

[10] R. Kleinman and P. M. van den Berg, "A modified gradient method for two-dimensional problems in tomography," *J. Comput. Appl. Math.*, vol. 42, no. 1, pp. 17–35, 1992.

[11] R. E. Kleinman and P. M. van den Berg, "An extended range-modified gradient technique for profile inversion," *Radio Sci.*, vol. 28, no. 5, pp. 877–884, Sep. 1993.

[12] R. Kleinman and P. M. van den Berg, "Two-dimensional location and shape reconstruction," *Radio Sci.*, vol. 29, no. 4, pp. 1157–1169, Aug. 1994.

[13] P. M. van den Berg and R. E. Kleinman, "A contrast source inversion method," *Inverse Problems*, vol. 13, no. 6, p. 1607, 1997.

[14] B. Kooij, M. Lambert, and D. Lesselier, "Nonlinear inversion of a buried object in transverse electric scattering," *Radio Sci.*, vol. 34, no. 6, pp. 1361–1371, Dec. 1999.

[15] O. Féron, B. Duchêne, and A. Mohammad-Djafari, "Microwave imaging of inhomogeneous objects made of a finite number of dielectric and conductive materials from experimental data," *Inverse Problems*, vol. 21, no. 6, p. S95, 2005.

[16] C. Yu, L.-P. Song, and Q. H. Liu, "Inversion of multi-frequency experimental data for imaging complex objects by a DTA–CSI method," *Inverse Problems*, vol. 21, no. 6, p. S165, 2005.

[17] Y. Wang and W. C. Chew, "An iterative solution of the two-dimensional electromagnetic inverse scattering problem," *Int. J. Imag. Syst. Technol.*, vol. 1, no. 1, pp. 100–108, 1989.

[18] W. C. Chew and Y. M. Wang, "Reconstruction of two-dimensional permittivity distribution using the distorted Born iterative method," *IEEE Trans. Med. Imag.*, vol. 9, no. 2, pp. 218–225, Jun. 1990.

[19] F. Li, Q. H. Liu, and L.-P. Song, "Three-dimensional reconstruction of objects buried in layered media using Born and distorted Born iterative methods," *IEEE Geosci. Remote Sens. Lett.*, vol. 1, no. 2, pp. 107–111, Apr. 2004.

[20] C. Gilmore, P. Mojabi, and J. LoVetri, "Comparison of an enhanced distorted Born iterative method and the multiplicative-regularized contrast source inversion method," *IEEE Trans. Antennas Propag.*, vol. 57, no. 8, pp. 2341–2351, Aug. 2009.

[21] F. Le Louër, "Fast spectral methods for the shape identification problem of a perfectly conducting obstacle," in *The Open Archive HAL*, Jan. 2013, pp. 1–16. [Online]. Available: https://hal.archives-ouvertes.fr/hal-00780379

[22] A. Qing, "Electromagnetic inverse scattering of multiple two-dimensional perfectly conducting objects by the differential evolution strategy," *IEEE Trans. Antennas Propag.*, vol. 51, no. 6, pp. 1251–1262, Jun. 2003.

[23] A. Qing, "Electromagnetic inverse scattering of multiple perfectly conducting cylinders by differential evolution strategy with individuals in groups (GDES)," *IEEE Trans. Antennas Propag.*, vol. 52, no. 5, pp. 1223–1229, May 2004.

[24] D. Colton and A. Kirsch, "A simple method for solving inverse scattering problems in the resonance region," *Inverse problems*, vol. 12, no. 4, p. 383, 1996.

[25] D. Colton, M. Piana, and R. Potthast, "A simple method using Morozov's discrepancy principle for solving inverse scattering problems," *Inverse Problems*, vol. 13, no. 6, p. 1477, 1997.

[26] S. N. Fata and B. B. Guzina, "A linear sampling method for near-field inverse problems in elastodynamics," *Inverse problems*, vol. 20, no. 3, p. 713, 2004.

[27] I. Catapano, F. Soldovieri, and L. Crocco, "On the feasibility of the linear sampling method for 3D GPR surveys," *Prog. Electromagn. Res.*, vol. 118, pp. 185–203, Jul. 2011.

[28] T. Arens, "Why linear sampling works," *Inverse Problems*, vol. 20, no. 1, p. 163, 2003.

[29] M. R. Eskandari, R. Safian, and M. Dehmollaian, "Three-dimensional near-field microwave imaging using hybrid linear sampling and level set methods in a medium with compact support," *IEEE Trans. Antennas Propag.*, vol. 62, no. 10, pp. 5117–5125, Oct. 2014.

[30] D. J. Daniels, *Ground Penetrating Radar*. Hoboken, NJ, USA: Wiley, 2005.

[31] M. G. Amin, *Through-the-Wall Radar Imaging*. Boca Raton, FL, USA: CRC Press, 2016.

[32] D. C. Munson, J. D. O'Brien, and W. K. Jenkins, "A tomographic formulation of spotlight-mode synthetic aperture radar," *Proc. IEEE*, vol. 71, no. 8, pp. 917–925, Aug. 1983.

[33] M. Fink, "Time-reversal mirrors," *J. Phys. D, Appl. Phys.*, vol. 26, no. 9, p. 1333, 1993.

[34] M. Fink *et al.*, "Time-reversed acoustics," *Rep. Prog. Phys.*, vol. 63, no. 12, p. 1933, 2000.

[35] G. Micolau and M. Saillard, "D.O.R.T. method as applied to electromagnetic subsurface sensing," *Radio Sci.*, vol. 38, no. 3, pp. 4-1–4-12, Jun. 2003.

[36] M. E. Yavuz and F. L. Teixeira, "Frequency dispersion compensation in time reversal techniques for UWB electromagnetic waves," *IEEE Geosci. Remote Sens. Lett.*, vol. 2, no. 2, pp. 233–237, Apr. 2005.

[37] D. Liu, J. Krolik, and L. Carin, "Electromagnetic target detection in uncertain media: Time-reversal and minimum-variance algorithms," *IEEE Trans. Geosci. Remote Sens.*, vol. 45, no. 4, pp. 934–944, Apr. 2007.

[38] M. E. Yavuz and F. L. Teixeira, "Space–frequency ultrawideband time-reversal imaging," *IEEE Trans. Geosci. Remote Sens.*, vol. 46, no. 4, pp. 1115–1124, Apr. 2008.

[39] A. E. Fouda and F. L. Teixeira, "Imaging and tracking of targets in clutter using differential time-reversal techniques," *Waves Random Complex Media*, vol. 22, no. 1, pp. 66–108, 2012.

[40] S. Bahrami, A. Cheldavi, and A. Abdolali, "Ultrawideband time-reversal imaging with frequency domain sampling," *IEEE Geosci. Remote Sens. Lett.*, vol. 11, no. 3, pp. 597–601, Mar. 2014.

[41] A. E. Fouda and F. L. Teixeira, "Statistical stability of ultrawideband time-reversal imaging in random media," *IEEE Trans. Geosci. Remote Sens.*, vol. 52, no. 2, pp. 870–879, Feb. 2014.

[42] A. J. Devaney, "Time reversal imaging of obscured targets from multistatic data," *IEEE Trans. Antennas Propag.*, vol. 53, no. 5, pp. 1600–1610, May 2005.

[43] E. A. Marengo and F. K. Gruber, "Subspace-based localization and inverse scattering of multiply scattering point targets," *EURASIP J. Adv. Signal Process.*, vol. 2007, no. 1, pp. 1–16, 2006.

[44] E. A. Marengo, F. K. Gruber, and F. Simonetti, "Time-reversal MUSIC imaging of extended targets," *IEEE Trans. Image Process.*, vol. 16, no. 8, pp. 1967–1984, Aug. 2007.

[45] D. Ciuonzo, G. Romano, and R. Solimene, "Performance analysis of time-reversal MUSIC," *IEEE Trans. Signal Process.*, vol. 63, no. 10, pp. 2650–2662, May 2015.

[46] I. Catapano, A. Randazzo, E. Slob, and R. Solimene, "GPR imaging via qualitative and quantitative approaches," in *Civil Engineering Applications of Ground Penetrating Radar*. New York, NY, USA: Springer, 2015, pp. 239–280.

[47] M. A. Anastasio, X. Pan, and E. Clarkson, "Comments on the filtered backprojection algorithm, range conditions, and the pseudoinverse solution," *IEEE Trans. Med. Imag.*, vol. 20, no. 6, pp. 539–542, Jun. 2001.

[48] P. Zhang, X. Zhang, and G. Fang, "Comparison of the imaging resolutions of time reversal and back-projection algorithms in EM inverse scattering," *IEEE Geosci. Remote Sens. Lett.*, vol. 10, no. 2, pp. 357–361, Mar. 2013.

[49] I. Catapano, L. Crocco, and T. Isernia, "On simple methods for shape reconstruction of unknown scatterers," *IEEE Trans. Antennas Propag.*, vol. 55, no. 5, pp. 1431–1436, May 2007.

[50] L. Crocco, I. Catapano, L. di Donato, and T. Isernia, "The linear sampling method as a way to quantitative inverse scattering," *IEEE Trans. Antennas Propag.*, vol. 60, no. 4, pp. 1844–1853, Apr. 2012.

[51] L. D. Donato, M. T. Bevacqua, L. Crocco, and T. Isernia, "Inverse scattering via virtual experiments and contrast source regularization," *IEEE Trans. Antennas Propag.*, vol. 63, no. 4, pp. 1669–1677, Apr. 2015.

[52] L. D. Donato and L. Crocco, "Model-based quantitative cross-borehole GPR imaging via virtual experiments," *IEEE Trans. Geosci. Remote Sens.*, vol. 53, no. 8, pp. 4178–4185, Aug. 2015.

[53] M. Rabbani, A. Tavakoli, and M. Dehmollaian, "A hybrid quantitative method for inverse scattering of multiple dielectric objects," *IEEE Trans. Antennas Propag.*, vol. 64, no. 3, pp. 977–987, Mar. 2016.

[54] L.-P. Song and Q. H. Liu, "Fast three-dimensional electromagnetic nonlinear inversion in layered media with a novel scattering approximation," *Inverse Problems*, vol. 20, no. 6, p. S171, Nov. 2004.

[55] W. Shin, "3D finite-difference frequency-domain method for plasmonics and nanophotonics," Ph.D. dissertation, Dept. Elect. Eng., Stanford Univ., Stanford, CA, USA, 2013.

[56] G. Oliveri, P. Rocca, and A. Massa, "A Bayesian-compressive-sampling-based inversion for imaging sparse scatterers," *IEEE Trans. Geosci. Remote Sens.*, vol. 49, no. 10, pp. 3993–4006, Oct. 2011.

[57] S. Sarvotham, D. Baron, M. Wakin, M. F. Duarte, and R. G. Baraniuk, "Distributed compressed sensing of jointly sparse signals," in *Proc. Asilomar Conf. Signals, Syst., Comput.*, Nov. 2005, pp. 1537–1541.

[58] J. Chen and X. Ho, "Theoretical results on sparse representations of multiple-measurement vectors," *IEEE Trans. Signal Process.*, vol. 54, no. 12, pp. 4634–4643, Dec. 2006.

[59] E. van den Berg and M. P. Friedlander, "Theoretical and empirical results for recovery from multiple measurements," *IEEE Trans. Inf. Theory*, vol. 56, no. 5, pp. 2516–2527, May 2010.

[60] E. van den Berg and M. P. Friedlander, "Probing the Pareto frontier for basis pursuit solutions," *SIAM J. Sci. Comput.*, vol. 31, no. 2, pp. 890–912, 2008.

[61] E. van den Berg and M. P. Friedlander, "Sparse optimization with least-squares constraints," *SIAM J. Optim.*, vol. 21, no. 4, pp. 1201–1229, 2011.

[62] R. Ward, "Compressed sensing with cross validation," *IEEE Trans. Inf. Theory*, vol. 55, no. 12, pp. 5773–5782, Dec. 2009.

[63] J. Zhang, L. Chen, P. T. Boufounos, and Y. Gu. (2016). "Cross validation in compressive sensing and its application of OMP-CV algorithm." [Online]. Available: https://arxiv.org/abs/1602.06373

[64] W. Shin. (2015). *MaxwellFDFD Webpage*. [Online]. Available: https://github.com/wsshin/maxwellfdfd

[65] R. P. Brent, *Algorithms for Minimization Without Derivatives*. Englewood Cliffs, NJ, USA: Englewood Cliffs, 1973.

[66] G. E. Forsythe, M. A. Malcolm, and C. B. Moler, *Computer Methods for Mathematical Computations*. Englewood Cliffs, NJ, USA: Prentice-Hall, 1976.

[67] P. M. van den Berg, A. Abubakar, and J. T. Fokkema, "Multiplicative regularization for contrast profile inversion," *Radio Sci.*, vol. 38, no. 2, pp. 1–10, 2003.
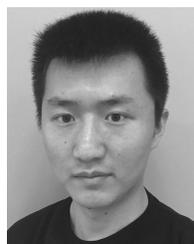
Shilong Sun received the B.S. and M.S. degrees in information and communication engineering from the National University of Defense Technology, Changsha, China, in 2011 and 2013, respectively. He is currently pursuing the Ph.D. degree with the Group of Microwave Sensing, Signals and Systems, Delft University of Technology, Delft, The Netherlands.

His research interests include inverse scattering problems and radar imaging.

Bert Jan Kooij was born in Amersfoort, The Netherlands, in 1959. He received the B.Sc. and M.Sc. degrees in electrical engineering and the Ph.D. degree in technical sciences from the Delft University of Technology, Delft, The Netherlands, in 1984, 1986, and 1994, respectively.

Since 1987, he has been a member of the Scientific Staff with the Electromagnetic Research Group, Delft University of Technology, where he has been involved in research and taught classes in the area of electromagnetics, acoustics, wave propagation, and scattering problems. In 1996, he was a Visiting Scientist with the École Supérieure d'Electricité - Supélec, Gif-sur-Yvette, France. He was involved in transient wave propagation problems in the field of elastodynamics and electromagnetics. His research interests include the computation of inverse wave-field problems employing iterative techniques based on error minimization and space time-domain wave-field modeling.

Dr. Kooij has been a member of the Microwave, Sensing, Signals and Systems Group, Delft University of Technology, since 2010.

Alexander G. Yarovoy (F'15) received the Diploma degree (Hons.) in radiophysics and electronics, the Cand.Phys. & Math.Sci. degree in radiophysics, and the Dr.Phys. & Math.Sci. degree in radiophysics from Kharkov State University, Kharkov, Ukraine, in 1984, 1987, and 1994, respectively.

In 1987, he joined as a Researcher with the Department of Radiophysics, Kharkov State University, where he became a Professor in 1997. From 1994 to 1996, he was with the Technical University of Ilmenau, Ilmenau, Germany, as a Visiting Researcher. Since 1999, he has been with the Delft University of Technology, Delft, The Netherlands. He has authored or co-authored over 250 scientific or technical papers and 14 book chapters, and holds four patents. His research interests include ultrawideband (UWB) microwave technology and its applications particularly radars and applied electromagnetics particularly UWB antennas. Prof. Yarovoy was a recipient of the European Microwave Week Radar Award for the paper that best advances the state of the art in radar technology in 2001 with L. P. Ligthart and P. van Genderen and in 2012 with T. Savelyev. In 2010, he was also a recipient of the Best Paper Award of the Applied Computational Electromagnetic Society with D. Caratelli. He has served as a Guest Editor of five Special Issues of the IEEE Transactions and other journals. Since 2011, he has been an Associated Editor of the *International Journal of Microwave and Wireless Technologies*. He has served as the Chair and Technical Program Committee (TPC) Chair at the fifth European Radar Conference (EuRAD 08), Amsterdam, The Netherlands, and the Secretary at the first European Radar Conference (EuRAD 04), Amsterdam. He has also served as the Co-Chair and TPC Chair at the tenth International Conference on Ground Penetrating Radar (GPR 2004), Delft. Since 2008, he has been the Director of the European Microwave Association. Since 2009, he has been the Chair of Microwave Sensing, Signals and Systems.